FROM ANALYSIS TO DESIGN OF HIGH-LIFT CONFIGURATIONS USING A NEWTON–KRYLOV ALGORITHM

Marian Nemec and David W. Zingg
University of Toronto Institute for Aerospace Studies
4925 Dufferin Street, Toronto, ON
Canada, M3H 5T6
marian@oddjob.utias.utoronto.ca

Keywords: *optimal shape design, airfoil, Navier–Stokes, high-lift, discrete gradient, adjoint, flow sensitivities, Newton's method, GMRES*

Abstract

An efficient multi-block Newton–Krylov algorithm using the compressible Navier–Stokes equations is presented for the analysis and design of high-lift airfoil configurations. The preconditioned generalized minimum residual (GMRES) method is applied to solve the discrete-adjoint equation, leading to a fast computation of accurate objective function gradients. Furthermore, the GMRES method is used in conjunction with an inexact-Newton approach to obtain fast solutions of the Navier–Stokes equations. Optimization constraints are enforced through a penalty formulation, and the resulting unconstrained problem is solved via a quasi-Newton method. Several design examples are provided which demonstrate that this algorithm provides an effective and practical tool for the design of multi-element airfoil configurations.

1 Introduction

The design of an efficient high-lift configuration can significantly improve the aerodynamic performance of an aircraft, as well as provide weight savings and reductions in the complexity of the high-lift system [27]. Consequently, the application of gradient-based optimization algorithms to the design of high-lift multi-element configurations is an active area of research [5, 7, 2, 11, 1, 19, 13]. This challenging optimization problem features complex geometry, with strict geometry constraints, and complex flow physics, such as regions of separated flow and confluent boundary layers and wakes.

A gradient-based algorithm for aerodynamic shape optimization problems can be divided into four modules: 1) an optimizer, 2) a flow solver, 3) a gradient computation algorithm, and 4) a grid-perturbation strategy. The accuracy of the optimization ultimately depends on the modeling of the flowfield, and hence, the flow solver. Accurate modeling of the complex flowfields encountered in high-lift problems requires the solution of the compressible Navier–Stokes equations in conjunction with a turbulence model. A detailed review of flow solvers and results for the prediction of high lift is provided by Rumsey and Ying [24].

For a given number of objective function and gradient evaluations, the efficiency of the optimization procedure is dominated by the time required to solve the flowfield equations and compute the gradient. In particular, significant computational effort is required to obtain accurate gradients. Generally, the cost of one gradient evaluation is equivalent to between one and two flowfield solutions [23, 18, 19, 11, 6, 12].

In [16], we presented an accurate and efficient algorithm for the calculation of the objective function gradient via the discrete-adjoint method. The adjoint equation is solved using the preconditioned generalized minimum residual (GMRES) Krylov subspace method [25]. Overall, the gradient is obtained in just one-fifth to one-half of the time required for a warm-started flow solution. The performance of the algorithm is demonstrated for several design examples, all based on single-element airfoils.

The objectives of this work are to extend and apply the Newton–Krylov algorithm presented in [16] to the analysis and design of high-lift multi-element configurations. The new algorithm is based on an established flow solver TORNADO [15, 9, 14]. The validation and performance of the new algorithm are demonstrated for lift-enhancement design examples based on a two-element take-off configuration.

2 Problem Formulation

The aerodynamic shape optimization problem consists of determining values of design variables X, such that the objective function $\mathcal{J}$ is minimized

$$\min_X \mathcal{J}(X,Q) \tag{1}$$

subject to constraint equations C_j,

$$C_j(X,Q) \leq 0 \qquad j=1,\ldots,N_c \tag{2}$$

where the vector Q denotes the conservative flowfield variables and N_c denotes the number of constraint equations. The flowfield variables are forced to satisfy the governing flowfield equations, $\mathcal{F}$, within a feasible region of the design space Ω,

$$\mathcal{F}(X,Q)=0 \qquad \forall\, X \in \Omega \tag{3}$$

which implicitly defines $Q=f(X)$.

The objective function is given by

$$\mathcal{J}=\begin{cases} \omega_L\left(1-\frac{C_L}{C_L^*}\right)^2+\omega_D\left(1-\frac{C_D}{C_D^*}\right)^2 & \text{if } C_D > C_D^* \\ \omega_L\left(1-\frac{C_L}{C_L^*}\right)^2 & \text{otherwise} \end{cases} \tag{4}$$

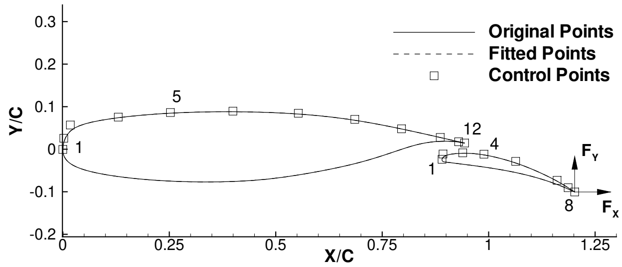

Fig. 1 B-spline curves and flap translation design variables

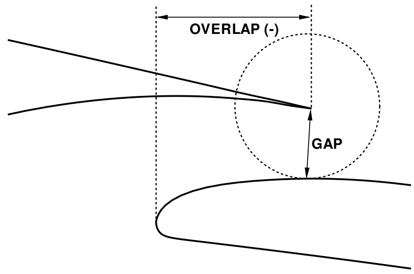

Fig. 2 Definition of gap and overlap distances

where C_D^* and C_L^* represent the target drag and lift coefficients, respectively. The weights ω_D and ω_L are user specified constants. This objective can be used for both lift-enhancement and lift-constrained drag minimization problems.

The design variables are based on a B-spline parameterization [3, 16] of the airfoil. An example is shown in Fig. 1, where a B-spline curve is fitted over the upper surface of the main element, and also the upper surface of the flap for the NLR 7301 configuration [28]. The vertical coordinates of the B-spline control points are used as design variables. Depending on the problem of interest, additional design variables may include the angle of attack, and the horizontal and vertical translation associated with each high-lift element in multi-element configurations, labeled as F_x and F_y in Fig. 1. The horizontal and vertical translation design variables control the gap and overlap distances in the slot region of the airfoil, as defined in Fig. 2.

The constraint equations, Eq. 2, represent airfoil thickness constraints that are used to ensure feasible designs. The constraints are given by

$$h^*(z_j)-h(z_j) \leq 0 \tag{5}$$

where $h^*(z_j)$ represents the minimum allowable thickness at location z_j expressed as a fraction of the airfoil's chord. For multi-element configurations, it is also necessary to constrain the gap and overlap distances. These constraints are required in order to prevent collisions among the elements and to ensure a reasonable computational grid.

The governing flow equations are the compressible two-dimensional thin-layer Navier–Stokes equations in generalized coordinates,

$$\frac{\partial \widehat{E}(\widehat{Q},X)}{\partial \xi} + \frac{\partial \widehat{F}(\widehat{Q},X)}{\partial \eta} = Re^{-1}\frac{\partial \widehat{S}(\widehat{Q},X)}{\partial \eta} \tag{6}$$

where $\widehat{Q} = J^{-1}Q = J^{-1}[\rho, \rho u, \rho v, e]^T$ is the vector of conservative dependent state variables, ξ and η are the streamwise and normal generalized coordinates, respectively, and J is the Jacobian of the coordinate transformation from Cartesian coordinates. Vectors $\widehat{E}$ and $\widehat{F}$ represent the convective flux vectors, the viscous flux vector is given by $\widehat{S}$, and Re denotes the Reynolds number. Sutherland's law is used to determine the laminar viscosity. The equations are in non-dimensional form. For further details, see [22]. The turbulent viscosity is modeled with the Spalart–Allmaras turbulence model [26]. All cases considered in this study are assumed to be fully turbulent, and therefore, the laminar-turbulent trip terms are not used.

3 Numerical Method

The aerodynamic shape optimization problem defined by Eqs. 1–3 is cast as an unconstrained problem. This is accomplished by lifting the side constraints, Eq. 2, into the objective function $\mathcal{J}$ using a penalty method. Furthermore, the constraint imposed by the flowfield equations, Eq. 3, is satisfied at every point within the feasible design space, and consequently these equations do not explicitly appear in the formulation of the optimization problem.

The unconstrained problem is solved using the BFGS quasi-Newton method in conjunction with a backtracking line search [20, 16]. At each step of the line search, the objective function value and gradient are required in order to construct a local cubic interpolant. Note that the optimization problem is based on the discrete form of the flowfield equations. Using the discrete approach, we expect the gradient to vanish at the optimum solution. In the following sections, we present the formulation for the penalized objective function, as well as the algorithms used for the flowfield evaluation (objective function value), the gradient evaluation, and the grid-perturbation strategy.

3.1 Objective with Constraints

A penalty method is used to combine the objective function with the constraint equations

$$\mathcal{J} = \mathcal{J}_O + \omega_T \sum_{j=1}^{N_c} C_j \tag{7}$$

where $\mathcal{J}_O$ refers to Eq. 4. The constraint equations represent thickness, gap, and overlap constraints, which are cast using a quadratic penalty term. For example, the thickness constraint, based on Eq. 5, is given by

$$C_j = \begin{cases} \left[1 - h(z_j)/h^*(z_j)\right]^2 & \text{if } h(z_j) < h^*(z_j) \\ 0 & \text{otherwise} \end{cases} \tag{8}$$

where ω_T is a user specified constant. A similar quadratic term is used to enforce the lower and upper bounds for the gap and overlap distances.

3.2 Flowfield Evaluation

The spatial discretization of the flowfield equations, Eq. 6, is the same as that used in TORNADO [15] (see also ARC2D [22]) for structured multi-block H-topology grids. The discretization consists of second-order centered-difference operators with second- and fourth-difference scalar artificial dissipation. The Spalart–Allmaras turbulence model is discretized as described in [26, 9]. Overall, the spatial discretization leads to a nonlinear system of equations

$$R(X, \widehat{Q}) = 0 \tag{9}$$

Although R is written as a function of the design variables, we emphasize that during a flowfield solution the design variables, and consequently the computational grid, are constants.

Eq. 9 is solved in a fully-coupled manner, where convergence to steady state is achieved using the preconditioned GMRES algorithm in conjunction with an inexact-Newton strategy [21, 16]. The main components include matrix-free GMRES(40) and a block-fill incomplete LU (BFILU) preconditioner. The matrix-vector products required at each GMRES iteration are formed with first-order finite-differences. Right preconditioning is used, and the preconditioner is based on an approximate-flow-Jacobian matrix. The level of fill for most cases is 2 [BFILU(2)], but difficult multi-element cases may require BFILU(4). The approximate-factorization algorithm [22, 15] is used to reduce the initial residual by three orders of magnitude in order to avoid Newton startup problems.

The approximate-flow-Jacobian matrix used for the preconditioner is identical to the flow-Jacobian matrix, $\partial R/\partial Q$, except for the treatment of the artificial-dissipation coefficients [16]. Hence, the preconditioner contains the contributions from all components of the residual vector, namely inviscid and viscous fluxes, boundary conditions, block interfaces, and the turbulence model. The artificial-dissipation coefficients, which include the spectral radius and the pressure switch, are assumed to be constant with respect to the flowfield variables. Furthermore, the preconditioning matrix is formed with only second-difference dissipation, but the second-difference coefficient is combined with the fourth-difference coefficient as follows,

$$d_l^{(2)} = d_r^{(2)} + \phi d_r^{(4)} \tag{10}$$

where the subscript r denotes the contribution from the right-hand side, and the subscript l denotes the resulting left-hand side value used in forming the preconditioner. This modification does not affect the steady-state solution. Fast convergence is obtained with the value of ϕ set to 6.0, which has been determined through numerical experiments.

Eq. 10 improves the diagonal dominance of the preconditioning matrix and reduces the work and storage requirements of the incomplete factorization. This approach is similar to the 'diagonal shift' strategy suggested by Chow and Saad [4]. The present preconditioning matrix is a compromise between a preconditioner based on a first-order upwind discretization of the flowfield equations and a preconditioner based on the actual second-order discretization. This novel 'intermediate' preconditioner is significantly more effective than either of these more commonly used approaches.

3.3 Gradient Evaluation

The gradient, $\mathcal{G}$, of the objective function $\mathcal{J}[X, Q(X)]$ is given by

$$\mathcal{G} = \frac{\mathrm{d}\mathcal{J}}{\mathrm{d}X} = \frac{\partial \mathcal{J}}{\partial X} + \frac{\partial \mathcal{J}}{\partial Q}\frac{\mathrm{d}Q}{\mathrm{d}X} \tag{11}$$

where we reduce the vector of design variables, X, to a scalar in order to clearly distinguish between partial and total derivatives. For problems with multiple design variables, it may be helpful to note that $\mathcal{G}$ and $\partial\mathcal{J}/\partial X$ are $[1 \times N_\mathrm{D}]$ row vectors, $\partial\mathcal{J}/\partial Q$ is a $[1 \times N_\mathrm{F}]$ row vector, and $\mathrm{d}Q/\mathrm{d}X$ is a $[N_\mathrm{F} \times N_\mathrm{D}]$ matrix, where N_D represents the number of design variables and N_F represents the number of flowfield variables. We assume that the implicit function $Q(X)$ is sufficiently smooth even in the presence of flow discontinuities such as shock waves. See [10, 8] for further details.

The difficulty in Eq. 11 is the evaluation of the term $\mathrm{d}Q/\mathrm{d}X$, referred to as the flow sensitivities. Evaluation of the partial derivatives, $\partial\mathcal{J}/\partial X$ and $\partial\mathcal{J}/\partial Q$, is relatively straightforward and is described at the end of this section. The flow sensitivities are obtained by differentiating the flowfield equations, Eq. 9, with respect to the design variables, which yields the following large system of linear equations

$$\frac{\partial R}{\partial Q}\frac{\mathrm{d}Q}{\mathrm{d}X} = -\frac{\partial R}{\partial X} \tag{12}$$

The direct, or flow-sensitivity, method results from solving Eq. 12 for the flow sensitivities $\mathrm{d}Q/\mathrm{d}X$ and using these values in Eq. 11 to obtain the gradient.

In order to formulate the discrete adjoint method, substitute Eq. 12 into Eq. 11 and define the following intermediate problem

$$\psi^{\mathrm{T}} = \frac{\partial \mathcal{J}}{\partial Q}\left(\frac{\partial R}{\partial Q}\right)^{-1} \tag{13}$$

where ψ is a $[N_{\mathrm{F}} \times 1]$ column vector. Post-multiplication of both sides by $\partial R/\partial Q$ and applying the transpose operator results in the following linear system of equations

$$\frac{\partial R}{\partial Q}^{\mathrm{T}} \psi = \frac{\partial \mathcal{J}}{\partial Q}^{\mathrm{T}} \tag{14}$$

This is known as the adjoint equation, and the vector ψ represents the adjoint variables. The expression for the gradient becomes

$$\frac{\mathrm{d}\mathcal{J}}{\mathrm{d}X} = \frac{\partial \mathcal{J}}{\partial X} - \psi^{\mathrm{T}}\frac{\partial R}{\partial X} \tag{15}$$

The GMRES strategy from the flow solver, discussed in Subsection 3.2, is adopted to solve both the adjoint and flow-sensitivity equations. Fast adjoint and flow-sensitivity solutions are obtained with BFILU(6), GMRES(85), and $\phi = 6.0$. For the flow-sensitivity equation, we use matrix-free GMRES. In addition to memory savings, the matrix-free approach is easier to implement, since an accurate differentiation of cumbersome functions in the residual equations, such as the absolute value and min / max functions, is 'automatically' provided. Due to the transpose on the left-hand-side of Eq. 14, the matrix-free approach is not possible for the adjoint equation. The flow-Jacobian matrix is stored explicitly, where we include the contribution from the spectral radius, but we treat the pressure switch associated with the artificial dissipation scheme as a constant.

The remaining terms in Eqs. 11 and 15, namely the objective function sensitivities $\partial\mathcal{J}/\partial X$ and $\partial\mathcal{J}/\partial Q$, as well as the residual sensitivity $\partial R/\partial X$, are evaluated using centered differences. The use of centered differences for the evaluation of the partial derivative terms is not computationally expensive. For example, the centered-difference formula for the residual sensitivities is given by

$$\frac{\partial R}{\partial X}_i = \frac{R(X + he_i, Q) - R(X - he_i, Q)}{2h} \tag{16}$$

where

$$h = \max\left(\varepsilon \cdot |X_i|, 1 \times 10^{-8}\right) \tag{17}$$

and $i = 1, \ldots, N_{\mathrm{D}}$. The ith unit vector is denoted by e_i, and a typical value of ε is 1×10^{-5}. It is important to realize that Eq. 16 involves two evaluations of only the residual vector per design variable and *not* two flowfield solutions. Note that the evaluation of residual sensitivities includes the evaluation of grid sensitivities, since the design variables do not explicitly appear in the residual equations except for the angle of attack design variable, see [16] for further details.

3.4 Grid-Perturbation Strategy

As the shape and position of an airfoil evolve during the optimization process, the location of the grid nodes is adjusted from the baseline configuration to conform to the new configuration. In [16], we use an algebraic grid-perturbation strategy that preserves the distance to the outer boundary and relocates the grid nodes in the normal direction proportional to the distance from the airfoil boundary. When the optimization problem involves the horizontal and vertical translation of a slat or a flap, the use of this strategy can result in significantly skewed grid cells near the boundary.

In order to improve the quality of the modified grid, we present a new grid-perturbation strategy given by

$$y_k^{\mathrm{new}} = y_k^{\mathrm{old}} + \frac{\Delta y}{2}\left[1 + \cos\left(\pi S_k\right)\right] \tag{18}$$

where Δy represents the airfoil shape change. S_k is the normalized arclength distance given by

$$S_k = \frac{1}{L_{\mathrm{g}}}\sum_{i=2}^{k} L_i \quad k = 2, \ldots, k_{\max} - 1 \tag{19}$$

where $S_1 = 0$, L_i is the length of a segment between nodes k and $k-1$, and L_{g} is the grid-line length from the body to the outer boundary. An evaluation of the new grid-perturbation strategy is presented in [17], where we demonstrate that the new strategy provides superior estimates of aerodynamic performance.

4 Validation

Before presenting design examples for high-lift configurations, we carefully validate the performance of the flow solver and the gradient computation algorithm. All grids for this and the following sections consist of approximately 31,000 nodes. The off-wall spacing is $2 \times 10^{-6}c$, the distance to the outer boundary is $12c$, the spacing at the H-topology grid stagnation points is $2 \times 10^{-5}c$, and the trailing-edge clustering is $2 \times 10^{-3}c$. The reported CPU times are obtained on a 667 MHz Alpha 21264 processor (SPECfp 2000 rating of 562 peak).

4.1 Flow-Solver Performance

A fast solution of the flowfield equations is a critical component of an effective design algorithm, since an evaluation of the objective function is required at each iteration of the optimizer. The performance of the flow solver is examined for the NLR 7301 configuration at $M_\infty = 0.25$, $\alpha = 8^\circ$ and $Re = 2.51 \times 10^6$. Fig. 3 shows that the Newton–Krylov flow solver (denoted as NK) is approximately two to three times faster than the approximate-factorization flow solver (denoted as AF). For many cases, this speed-up can be even larger. Initially, the convergence rate of both flow solvers is identical, since approximate-factorization is used as a startup procedure for the Newton–Krylov flow solver.

One of the main difficulties associated with Newton's method is the startup procedure. The Newton–Krylov flow solver is particularly well suited for the design problem since once we obtain the solution for the initial airfoil shape, we warm-start the remaining flow solves. If the step-sizes during the line-search procedure are sufficiently small, the startup procedure using approximate factorization is not necessary. The warm-started flow solves typically converge in 2/3 of the original flow solve time.

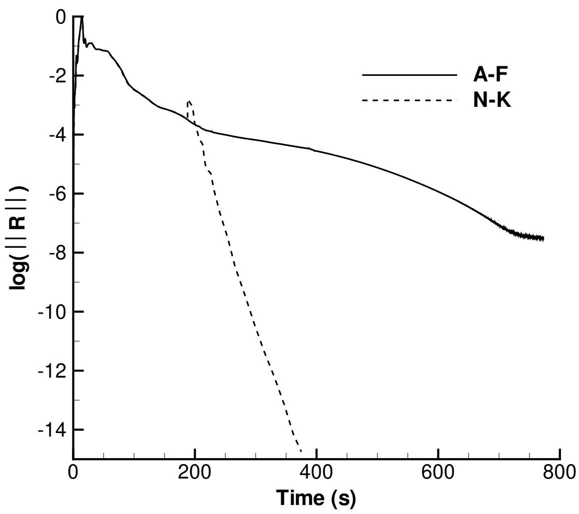

Fig. 3 Flow-solver performance

4.2 Gradient Accuracy

Finite-difference gradients provide a benchmark that is used to establish the accuracy of the gradient computation using the flow-sensitivity and adjoint methods. A subsonic lift-enhancement problem for the NLR 7301 configuration is considered. During the computation of the finite-difference gradient, the flowfield solution is converged 14 orders of magnitude. The flow-sensitivity and adjoint equations are converged 8 orders of magnitude.

The freestream conditions are $M_\infty = 0.25$, $\alpha = 4^\circ$, and $Re = 2.51 \times 10^6$. We compute the gradient of the objective function, Eq. 4, with respect to control point 5 on the main airfoil (denoted as 5M), control point 4 on the flap (denoted as 4F), and the horizontal and vertical flap displacements (denoted as F_x and F_y, respectively), see Fig. 1. The target drag coefficient, C_D^*, is set equal to the initial drag coefficient, while the target lift coefficient, C_L^*, is set equal to 2.2, which represents a 2.5% increase from the initial value. The values of ω_L and ω_D in Eq. 4 are both set to 1.0 and there are no side constraints. Table 1 shows that there is an excellent agreement between the finite-difference, adjoint, and flow-

Table 1 Gradient accuracy

Design Variable	Finite Difference	Adjoint (% Diff.)[b]	S-MF[a] (% Diff.)[b]
5M	-0.01228	0.02	-0.07
4F	-0.08533	-0.19	-0.07
F_x	-0.02591	0.06	-0.02
F_y	-0.03363	-0.05	-0.05

[a] matrix-free flow-sensitivity
[b] $\% \text{ Diff} = (\mathcal{G} - \mathcal{G}_{\text{FD}})/\mathcal{G}_{\text{FD}} \times 100$

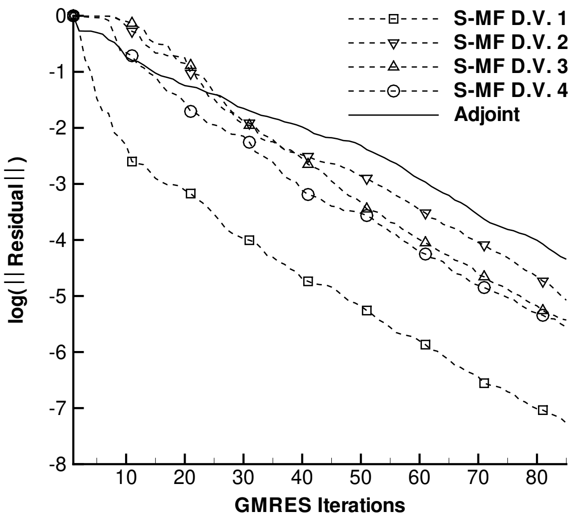

Fig. 4 GMRES convergence (S-MF denotes matrix-free flow-sensitivity, D.V. denotes design variable)

sensitivity gradients.

4.3 Gradient Computation Efficiency

Fig. 4 shows the convergence of the adjoint and flow-sensitivity equations for the lift-enhancement problem introduced in the previous subsection. The residuals of the flow-sensitivity equation are shown for each design variable. Fig. 4 highlights the influence of different right-hand-side vectors on the convergence of GMRES(85). Note that the initial guess for the adjoint and flow-sensitivity solution vectors is zero. The left-hand side of the flow-sensitivity equation, Eq. 12, is the flow-Jacobian matrix. This matrix remains the same for each design variable. For the adjoint equation, Eq. 14, the left-hand side is the transpose of the flow-Jacobian matrix. The transpose operator does not change the eigenvalues of the flow Jacobian. Although the flow-sensitivity equation converges faster than the adjoint equation, the flow-sensitivity equation must be solved for each design variable, resulting in a much longer gradient computation time.

Fig. 5 compares the convergence history of the adjoint and flowfield equations with respect to CPU time. The time for the formation of the preconditioning matrices is included in Fig. 5.[1] It is necessary to converge the adjoint equation only three orders of magnitude in order to obtain gradients of sufficient accuracy [23, 18, 12]. This level of convergence is achieved in approximately 45 seconds, as shown in Fig. 5. For the flowfield equations, we typically reduce the residual by ten orders of magnitude in order to prevent stalling of the line searches once the solution is close to the optimum. This convergence level is achieved in 245 seconds, and consequently, the gradient is obtained in less than one-fifth of the flow solve time.

[1] In Fig. 5, the 'flat step' in the convergence of the flow solver after a three order-of-magnitude decrease in the residual indicates the formation time of the preconditioner. For the adjoint equation, this time is indicated at the start of the convergence history.

5 Design Examples

5.1 Flap Position Optimization

The goal of this design example is to determine the optimal gap and overlap distances for the NLR 7301 configuration, such that the resulting configuration achieves a higher lift coefficient while maintaining the same (or lower) drag coefficient. The freestream conditions are specified in Subsection 4.2. The initial values of C_L and C_D are 2.145 and 0.04720, respectively. The objective function is given by Eq. 4, where we set $C_L^* = 2.180$ and C_D^* equal to the initial drag coefficient. The weights ω_L and ω_D are set to 1.0. The design variables are the horizontal and vertical

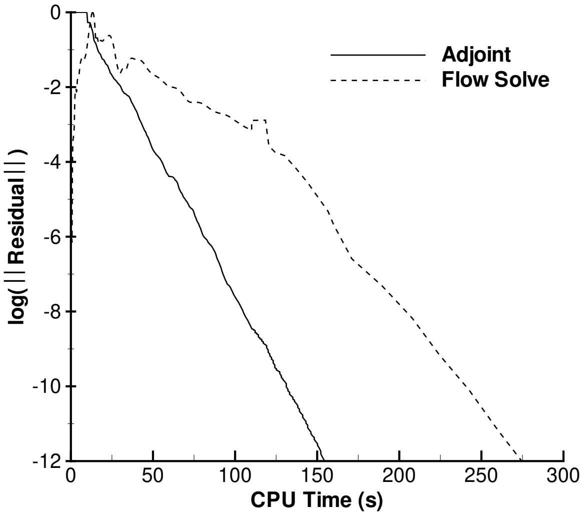

Fig. 5 Comparison of adjoint and flow solve convergence times

Table 2 Gap-overlap optimization summary

Design	C_L	C_D	G[a]	O[b]
NLR 7301	2.145	0.04720	2.40	-5.31
#1	2.165	0.04687	1.99	-4.28
#2	2.173	0.04677	1.95	-3.30
Final	2.175	0.04675	2.02	-2.68
Target	2.180	≤ 0.0472		

[a] Gap $(\%c)$
[b] Overlap $(\%c)$

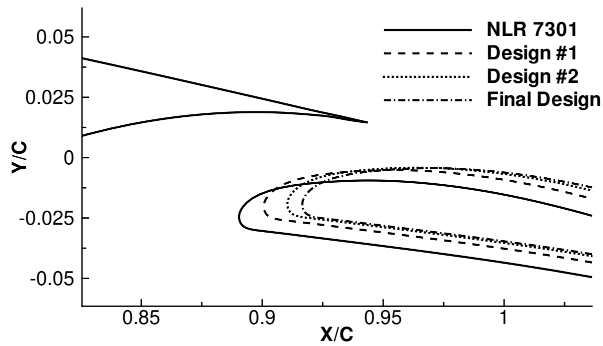

Fig. 6 Flap position summary

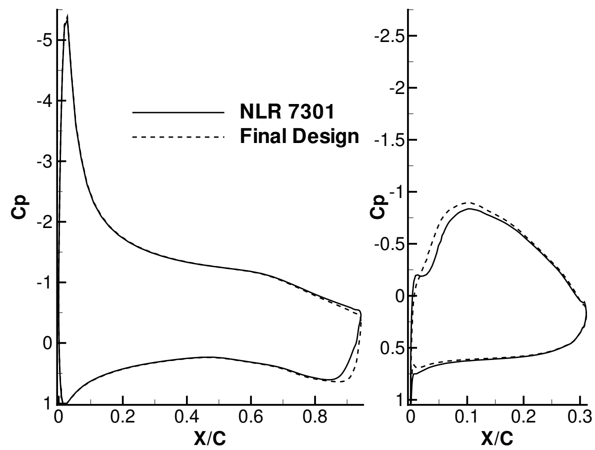

Fig. 7 C_p distribution for main element and flap

displacements of the trailing edge of the flap, as indicated in Fig. 1. The gap and overlap limits are set to $\pm 0.5\%c$ and $\pm 1.0\%c$, respectively, based on the initial configuration. The weight, ω_T, associated with the gap and overlap constraints is set to 0.05. The gradient is computed using the adjoint method.

Table 2 and Fig. 6 summarize the results. Within a few flowfield and gradient evaluations, the flap reaches the maximum allowable overlap distance of approximately $-4.3\%c$, at which point the overlap penalty function becomes active. The optimization converges to the design #1 configuration, shown in Fig. 6. A new grid is generated for this configuration and the corresponding values of C_L and C_D are given in Table 2. The optimization is restarted from the new grid with the same objective function. This procedure is continued until convergence to the final design is obtained (see Fig. 6), where the gap and overlap constraints are no longer active. Note that the drag objective is satisfied for all the designs. Consequently, the optimization is purely attempting to maximize the lift coefficient. Overall, a 1.4% increase in the value of the lift coefficient is obtained. This is achieved by an increased loading on the main element as well as the flap, as shown in Fig. 7.

Example convergence histories for the design

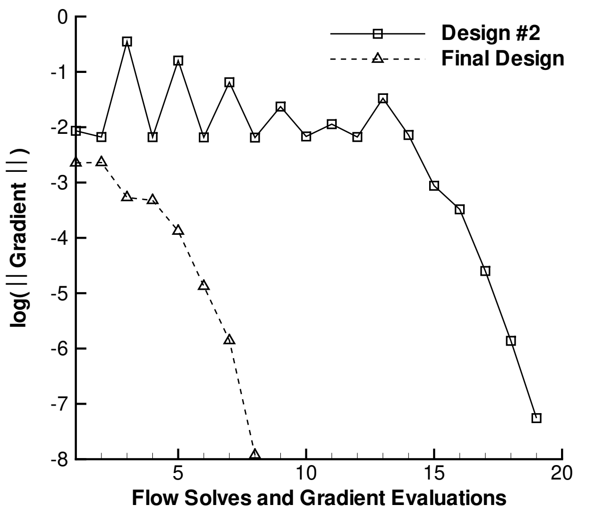

Fig. 8 Convergence histories for gap-overlap optimization

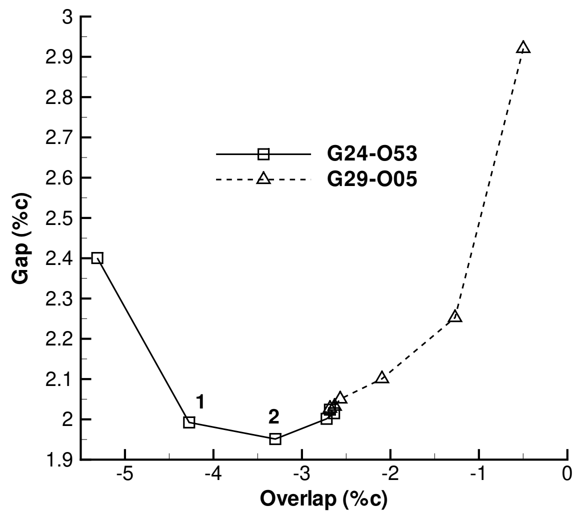

Fig. 9 Convergence to optimal gap-overlap distances from two distinct initial conditions

#2 and final configurations are shown in Fig. 8. The oscillations in the L_2 norm of the gradient for design #2 are due to the presence of the gap and overlap constraints. The norm of the gradient is reduced by several orders of magnitude, which indicates that the optimization converged to a local minimum.

Given that the target value of the lift coefficient is not achieved at the final design configuration (see Table 2), it is somewhat surprising that further design improvements cannot be realized by further extending the effective chord of the configuration. The convergence of the gradient in Fig. 8 indicates that a local optimum has been found, but a global optimum is not guaranteed. In order to verify the uniqueness of the optimal solution, the optimization is restarted from a different initial condition. The flap is re-positioned to a gap of 2.9%c and an overlap of -0.5%c, i.e., the leading edge of the flap is almost aligned with the trailing edge of the main element. Fig. 9 shows that the optimization converges to the same optimum solution. The data labeled 'G24-O53' show the convergence to the optimum solution from the original configuration, with designs #1 and #2 indicated, while the data labeled 'G29-O05' show the convergence to the same optimum solution from the new initial conditions.

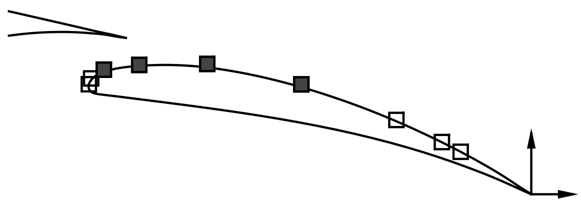

Fig. 10 Flap shape and position design variables

5.2 Flap Shape and Position Optimization

The flap position optimization example presented in Subsection 5.1 is expanded to include flap shape changes. As shown in Fig. 10, a B-spline curve is fitted over a portion of the upper surface of the flap, such that the cruise (flap-stowed) configuration is not affected by the shape modifications. The design variables consist of the four shaded control points, as well as the horizontal and vertical flap displacements.

The objective function and all the optimization parameters remain unchanged from Subsection 5.1 except for the target lift coefficient, which is increased to 2.2. Table 3 and Fig. 11 summarize the results. The optimization is started from the optimal gap and overlap values obtained previously, which is denoted as the initial configuration in Table 3 and Fig. 11. For the

Table 3 Flap optimization summary

Design	C_L	C_D	G[a]	O[b]
NLR 7301	2.145	0.04720	2.40	-5.31
Initial	2.175	0.04675	2.02	-2.68
Final	2.2	0.04723	2.06	-2.40
Target	2.2	≤ 0.0472		

[a] Gap $(\%c)$
[b] Overlap $(\%c)$

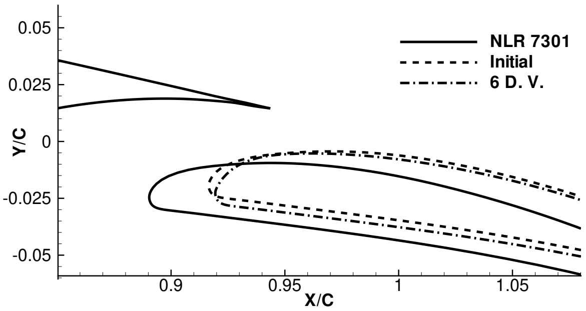

Fig. 11 Flap shape and position summary (D.V. denotes design variable)

final design, the gap distance remains approximately constant, but the thickness of the flap increases considerably near the leading edge, as shown in Fig. 11. The optimization converges in 25 flowfield and gradient evaluations. A new grid is generated for the final configuration, and the corresponding values of the lift and drag coefficients are provided in Table 3. Overall, the final design achieves a 2.5% increase in the lift coefficient value while almost no drag penalty is incurred when compared with the original NLR 7301 configuration. The pressure distributions for the main element and flap are shown in Fig. 12.

6 Conclusions

A Newton–Krylov algorithm for the analysis and design of multi-element airfoil configurations has been presented. The accuracy of the objective function gradient, based on the discrete-adjoint and flow-sensitivity methods, is excellent. Furthermore, the gradient is obtained in approximately one-fifth of the flow solve time when using the adjoint method. Overall, the results indicate that the new algorithm provides an efficient and robust tool for complex aerodynamic design problems.

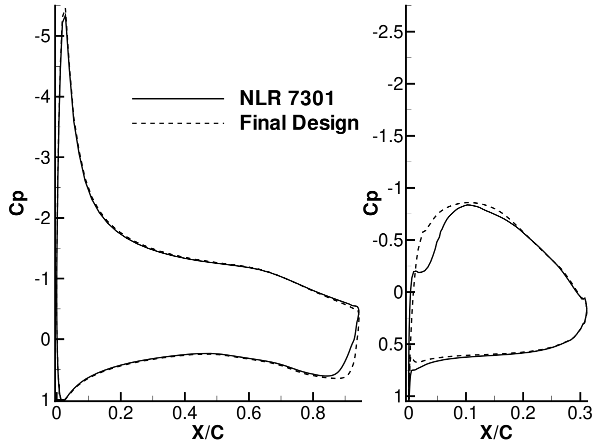

Fig. 12 C_p distribution for main element and flap

Acknowledgments

This research was supported by the Natural Sciences and Engineering Research Council of Canada, as well as Bombardier Aerospace and an OGS grant from the Government of Ontario.

References

[1] Alexandrov NM, Nielsen EJ, Lewis RM, and Anderson WK. First-order model management with variable-fidelity physics applied to multi-element airfoil optimization. AIAA Paper 2000–4886, September 2000.

[2] Anderson WK and Bonhaus DL. Airfoil design on unstructured grids for turbulent flows. *AIAA Journal*, Vol. 37, No 2, pp 185–191, 1999.

[3] Anderson WK and Venkatakrishnan V. Aerodynamic design optimization on unstructured grids with a continuous adjoint formulation. *Computers & Fluids*, Vol. 28, pp 443–480, 1999.

[4] Chow E and Saad Y. Experimental study of ILU preconditioners for indefinite matrices. *Journal of Computational and Applied Mathematics*, Vol. 86, pp 387–414, 1997.

[5] Drela M. Design and optimization method for

multi-element airfoils. AIAA Paper 93–0969, 1993.

[6] Elliott JK and Peraire J. Aerodynamic optimization on unstructured meshes with viscous effects. AIAA Paper 97–1849, June 1997.

[7] Eyi S, Lee KD, Rogers SE, and Kwak D. High-lift design optimization using Navier–Stokes equations. *Journal of Aircraft*, Vol. 33, No 3, pp 499–504, 1996.

[8] Giles MB and Pierce NA. An introduction to the adjoint approach to design. *Flow, Turbulence and Combustion*, Vol. 65, No 3/4, pp 393–415, 2000.

[9] Godin P, Zingg DW, and Nelson TE. High-lift aerodynamic computations with one- and two-equation turbulence models. *AIAA J.*, Vol. 35, No 2, pp 237–243, 1997.

[10] Gunzburger MD. Introduction into mathematical aspects of flow control and optimization. *Inverse Design and Optimization Methods*, Brussels, Belgium, April 1997. von Kármán Institute For Fluid Dynamics.

[11] Kim CS, Kim C, and Rho OH. Sensitivity analysis for the Navier–Stokes equations with two-equation turbulence models. *AIAA J.*, Vol. 39, No 5, pp 838–845, 2001.

[12] Kim H-J, Sasaki D, Obayashi S, and Nakahashi K. Aerodynamic optimization of supersonic transport wing using unstructured adjoint method. *AIAA Journal*, Vol. 39, No 6, pp 1011–1020, 2001.

[13] Kim S, Alonso JJ, and Jameson A. Design optimization of high–lift configurations using a viscous continuous adjoint method. AIAA Paper 2002–0844, January 2002.

[14] Nelson TE, Godin P, De Rango S, and Zingg DW. Flow computations for a three-element airfoil system. *Canadian Aeronautics and Space Journal*, Vol. 45, No 2, pp 132–139, 1999.

[15] Nelson TE, Zingg DW, and Johnston GW. Compressible Navier–Stokes computations of multielement airfoil flows using multiblock grids. *AIAA J.*, Vol. 32, No 3, pp 506–511, 1994.

[16] Nemec M and Zingg DW. Newton–Krylov algorithm for aerodynamic design using the Navier–Stokes equations. *AIAA J.*, Vol. 40, No 6, pp 1146–1154, 2002.

[17] Nemec M and Zingg DW. A Newton–Krylov algorithm for complex aerodynamic design. *Proc 10th Annual Conference of the CFD Society of Canada*, Windsor, ON, June 2002.

[18] Nielsen EJ. *Aerodynamic Design Sensitivities on an Unstructured Mesh Using the Navier Stokes Equations and a Discrete Adjoint Formulation*. PhD thesis, Virginia Polytechnic Institute and State University, 1998.

[19] Nielsen EJ and Anderson WK. Recent improvements in aerodynamic design optimization on unstructured meshes. *AIAA J.*, Vol. 40, No 6, pp 1155–1163, 2002.

[20] Nocedal J and Wright SJ. *Numerical Optimization*. Springer–Verlag Inc., New York, 1999.

[21] Pueyo A and Zingg DW. Efficient Newton–Krylov solver for aerodynamic computations. *AIAA J.*, Vol. 36, No 11, pp 1991–1997, 1998.

[22] Pulliam TH. Efficient solution methods for the Navier-Stokes equations. Technical report, Lecture Notes for the von Kármán Inst. for Fluid Dynamics Lecture Series, Brussels, Belgium, January 1986.

[23] Reuther JJ, Jameson A, Alonso JJ, Rimlinger MJ, and Saunders D. Constrained multipoint aerodynamic shape optimization using an adjoint formulation and parallel computers, part 2. *Journal of Aircraft*, Vol. 36, No 1, pp 61–74, 1999.

[24] Rumsey CL and Ying SX. Prediction of high lift: Review of present CFD capability. *Progress in Aerospace Sciences*, Vol. 38, No 2, pp 145–180, 2002.

[25] Saad Y and Schultz MH. GMRES: A generalized minimal residual algorithm for solving nonsymmetric linear systems. *SIAM J. Sci. & Stat. Comput.*, Vol. 7, No 3, pp 856–869, 1986.

[26] Spalart PR and Allmaras SR. A one-equation turbulence model for aerodynamic flows. AIAA Paper 92–0439, January 1992.

[27] Van Dam CP. The aerodynamic design of multi-element high-lift systems for transport airplanes. *Progress in Aerospace Sciences*, Vol. 38, No 2, pp 101–144, 2002.

[28] Van Den Berg B. Boundary layer measurements on a two-dimensional wing with flap. NLR TR 79009 U, January 1979.